

RESEARCH ARTICLE | JANUARY 21 2025

Proportions of incommensurate, resonant, and chaotic orbits for torus maps

E. Sander   ; J. D. Meiss 



Chaos 35, 013147 (2025)

<https://doi.org/10.1063/5.0226617>



View
Online



Export
Citation

Articles You May Be Interested In

KoopmanLab: Machine learning for solving complex physics equations

APL Mach. Learn. (September 2023)

Experimental realization of a quantum classification: Bell state measurement via machine learning

APL Mach. Learn. (September 2023)

Proportions of incommensurate, resonant, and chaotic orbits for torus maps

Cite as: Chaos 35, 013147 (2025); doi: 10.1063/5.0226617

Submitted: 2 July 2024 · Accepted: 6 January 2025 ·

Published Online: 21 January 2025



View Online



Export Citation



CrossMark

E. Sander^{1,a)} and J. D. Meiss^{2,b)}

AFFILIATIONS

¹Department of Mathematical Sciences, George Mason University, Fairfax, Virginia 22030, USA

²Department of Applied Mathematics, University of Colorado, Boulder, Colorado 80309-0526, USA

^{a)}Author to whom correspondence should be addressed: esander@gmu.edu

^{b)}Electronic mail: jdm@colorado.edu

ABSTRACT

This paper focuses on distinguishing classes of dynamical behavior for one- and two-dimensional torus maps, in particular, between orbits that are incommensurate, resonant, periodic, or chaotic. We first consider Arnold's circle map, for which there is a universal power law for the fraction of nonresonant orbits as a function of the amplitude of the nonlinearity. Our methods give a more precise calculation of the coefficients for this power law. For two-dimensional torus maps, we show that there is no such universal law for any of the classes of orbits. However, we find different categories of maps with qualitatively similar behavior. Our results are obtained using three fast and high precision numerical methods: weighted Birkhoff averages, Farey trees, and resonance orders.

Published under an exclusive license by AIP Publishing. <https://doi.org/10.1063/5.0226617>

We study nonlinear one- and two-dimensional torus maps, starting with Arnold's circle map.¹ Jensen and Ecke and their collaborators^{2,3} showed that the proportion of parameters for which the map has a dense orbit on the circle is given by a power law as a function of the amplitude of the nonlinearity, up to a critical amplitude where the map becomes noninvertible. We compute the power law parameters with higher accuracy. We then classify orbit types for 2D torus maps with typical nonlinearities. Grebogi *et al.*^{4,5} considered such maps but were only able to give relatively imprecise results. With improved numerical techniques, we show that there is no universal power law for the proportion of regular, nonresonant orbits, in contrast to the 1D case. Instead, we find several categories of nonlinearities for which there are different behaviors.

I. INTRODUCTION

The distinction between regular and chaotic orbits is fundamental to the study of dynamical systems. In this paper, we use the efficient and accurate method of weighted Birkhoff averages (WBAs)^{6–10} to distinguish between these classes of orbits by differences in the rate of convergence of the average. The WBA can also compute frequency vectors of regular orbits with high accuracy.

We previously used this to distinguish between rational and commensurate rotation vectors using Farey trees⁹ and resonance orders¹⁰ for area- and volume-preserving maps. In the current paper, we study maps on the torus and show that these three methods lead to a precise and efficient classification of their orbits as chaotic, resonant, or incommensurate.

Other methods for computing rotation numbers include Laskar's frequency analysis technique,¹¹ which uses a Hann window to improve Fourier analysis. It is important to note that Das and Yorke¹² proved that the WBA is super-convergent when the dynamics is analytically conjugated to a rigid rotation and the rotation number is a Diophantine irrational, while frequency analysis is only quadratically convergent. Another technique uses Richardson extrapolation,^{13–17} while this appears numerically to be super-convergent, we are not aware of a proof. Convergence rates have also been used by Rmaileh¹⁸ to distinguish between regular and chaotic behavior. More generally, MacKay¹⁹ showed that one can compute rotation intervals from a time series and Alseda and Borros-Cullell²⁰ did this for analytically known circle maps. Polotzek *et al.*²¹ computed rotation sets of torus maps using set based methods. Other approaches include numerical continuation of invariant tori²² and explicitly computing the conjugacy to rigid rotation.^{23,24} For a comparison of some of these methods to the WBA, see the discussion in Das *et al.*⁷

The paper proceeds as follows. In Sec. II, we give an overview of the theoretical background. In Sec. III and IV, we apply these methods to maps $f: \mathbb{T}^d \rightarrow \mathbb{T}^d$ for $d = 1$ and 2. We end with conclusions and future plans in Sec. V. The numerical methods we use, which have been developed in other papers, are described in Appendix A. Appendix B shows how to compute the critical amplitude for non-invertibility for $d = 2$, which we use in Sec. IV. Finally, Appendix C lists the parameters that we have used in our numerical simulations.

II. TORUS MAPS AND ROTATION VECTORS

We will consider maps $f: \mathbb{T}^d \rightarrow \mathbb{T}^d$ that are homotopic to the identity. In general, we can assume that f has the form

$$x' = f(x) = x + \Omega + g(x; a) \pmod{1} \quad (1)$$

where $\Omega \in \mathbb{T}^d$, a is a parameter vector, and the nonlinear term g is periodic, $g(x + m; a) = g(x; a)$ for any $m \in \mathbb{Z}^d$ (for every parameter a). We will study several simple examples. In Sec. III, we consider Arnold's circle map, where $d = 1$, and

$$g(x; a) = \frac{a}{2\pi} \sin(2\pi x). \quad (2)$$

In Sec. IV, we consider the fully 2D case, where $d = 2$, and g_1 and g_2 are both sums of sinusoidal functions. In all cases,

$$g(x; a) = 0 \text{ for } a = 0,$$

so that the dynamics of (1) then reduces to a rigid rotation on \mathbb{T}^d ,

$$x(t) = f^t(x(0)) = x(0) + t\Omega \pmod{1}, (a = 0),$$

in which case Ω becomes the frequency or rotation vector.

More generally, to determine the rotation vector for an orbit, we can lift f to \mathbb{R}^d using the standard projection $\pi: \mathbb{R}^d \rightarrow \mathbb{T}^d$. A map $F: \mathbb{R}^d \rightarrow \mathbb{R}^d$ is then a lift of f if

$$\pi \circ F = f \circ \pi.$$

Here, we take the periods of the torus to be one so that $F(x) \pmod{1} = f(x \pmod{1})$. Since f is homotopic to the identity, $F(x + m) = F(x) + m$ for each $m \in \mathbb{Z}^d$, i.e., the map acts trivially on the first homology group of the torus. Note that any two lifts, say, F_1 and F_2 , differ by an integer vector $F_1(x) = F_2(x) + m$ —indeed this must be true for any fixed x , but by continuity the same vector m must work for all x .

The orbit of $x \in \mathbb{T}^d$ has rotation vector $\omega \in \mathbb{T}^d$ if the limit

$$\omega(x, f) = \lim_{t \rightarrow \infty} \frac{F^t(x) - x}{t} \pmod{1} \quad (3)$$

exists. This is independent of the choice of lift; however, it can depend upon the initial point. More general versions of rotation vectors can be defined,^{25,26} and sometimes computed,^{20,21} but we will only compute (3).

For homeomorphisms of the circle ($d = 1$), Poincaré proved that strict monotonicity implies that the limit (3) exists and is independent of x . For the form (1), this occurs when $|g'(x; a)| \leq 1$ for all $x \in \mathbb{T}$. It is not hard to show that the resulting rotation number ω is a nondecreasing function of Ω . A circle map f that is smooth and strictly monotonic is a diffeomorphism, and, if f is sufficiently

regular, Denjoy showed that it is topologically conjugate to a rigid rotation when ω is irrational.^{27,28}

Even when $d > 1$ the dynamics of (1) can be conjugated to a rigid rotation only if it is a homeomorphism.⁵ Indeed, suppose that there exists a homeomorphism $\Phi: \mathbb{T}^d \rightarrow \mathbb{T}^d$ such that

$$f \circ \Phi = \Phi \circ R, \quad (4)$$

where $R(\theta) = \theta + \omega$ is the rigid translation on \mathbb{T}^d . Since $f = \Phi \circ R \circ \Phi^{-1}$ is a composition of homeomorphisms, it must be one as well. Moreover, if f and Φ are diffeomorphisms, then upon differentiation,

$$Df(x) = D\Phi(\Phi^{-1}(x) + \omega)D\Phi^{-1}(x);$$

therefore, $\det(Df) \neq 0$ for all x . This gives the necessary conditions.

Lemma 1. *If the map (1) is diffeomorphically conjugate to rigid rotation, then its Jacobian is nonsingular.*

The converse is—apparently—not true when $d > 1$.²⁹ Moreover, nonsingularity of Df , implying that f is a local diffeomorphism, does not imply that f is a global diffeomorphism. (This is related to the Jacobian conjecture, which has not even been proven for polynomials when the degree is larger than two.³⁰)

III. ARNOLD'S CIRCLE MAP

In this section, we study the Arnold¹ circle map; that is, we consider (1) for $d = 1$ with (2). This family of maps has two parameters, (Ω, a) , and without loss of generality we can assume that $\Omega \in [0, 1]$ and $a \geq 0$. The results are depicted in Figs. 1–3, and we quickly summarize them here. Figure 1 shows histograms of the precision, dig_T , see (A4) in Appendix A 1; the peaks near $\text{dig}_T \gtrsim 14$ correspond to

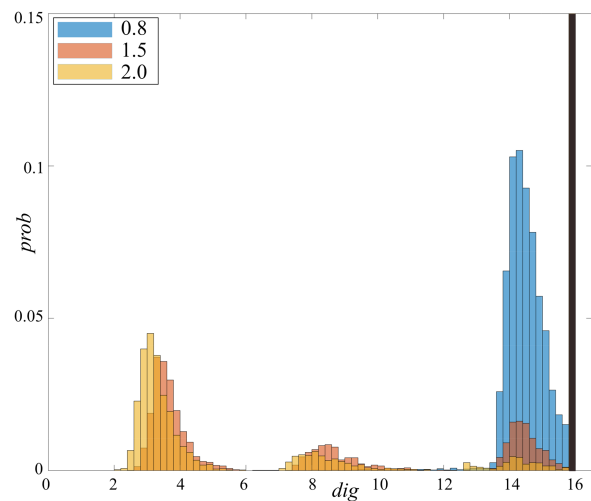


FIG. 1. Histograms of dig_T (A4) for the Arnold circle map (1) with (2), for ω_{10^5} using a grid of 10^4 values of $\Omega \in [0, 1]$. Three histograms are shown, $a = 0.8$ (blue), 1.5 (orange), and 2.0 (yellow). If the difference between the two averages in (A4) is no more than 10^{-16} , we set $\text{dig}_T = 16$. Each distribution has a peak at $\text{dig}_T = 16$ (black); these are truncated in the figure and have heights 0.35, 0.65, and 0.68, respectively.

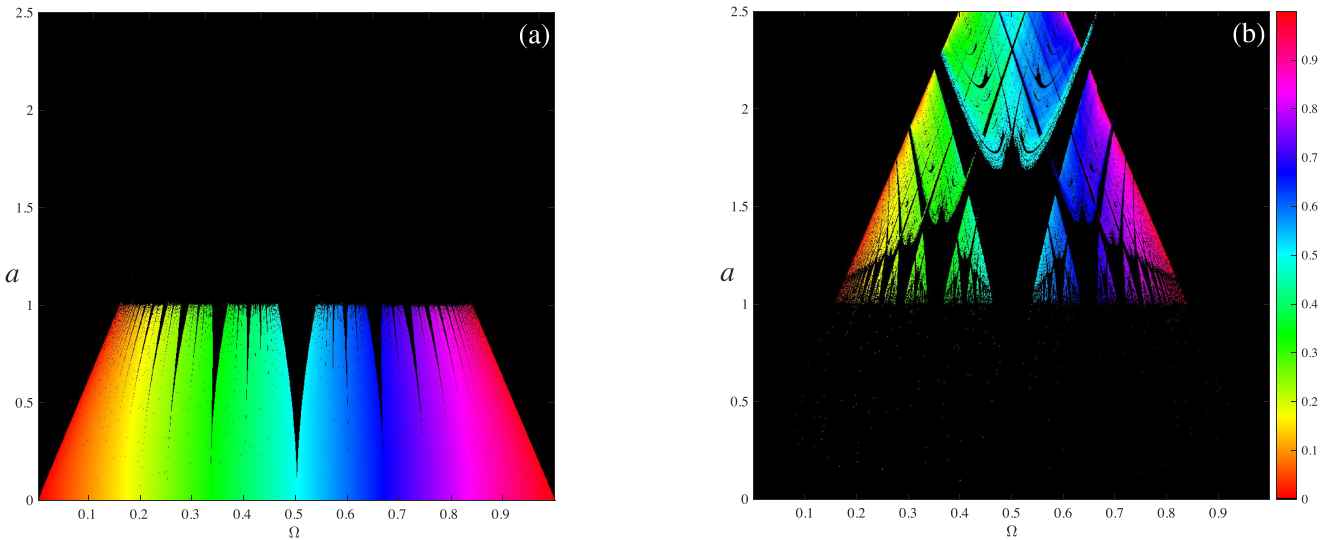


FIG. 2. Rotation number for the Arnold circle map (2) as a function of the parameters (Ω, a) . The color indicates ω , and black indicates no orbits of the given type. Panel (a) shows the nonresonant regular orbits and panel (b) the chaotic orbits.

nearly double precision accuracy for ω_T (A8) using $T = 10^5$ iterates. The panels of Fig. 2 categorize the behavior of orbits for $\Omega \in [0, 1]$ and $a \in [0, 2.5]$ with colors corresponding to ω_T . Parameters with orbits identified as quasiperiodic using (A15) are shown in Fig. 2(a) and those identified as chaotic using (A6) in Fig. 2(b). These data are used to produce Fig. 3, which shows the proportion of chaotic, periodic, and quasiperiodic orbits as a function of a .

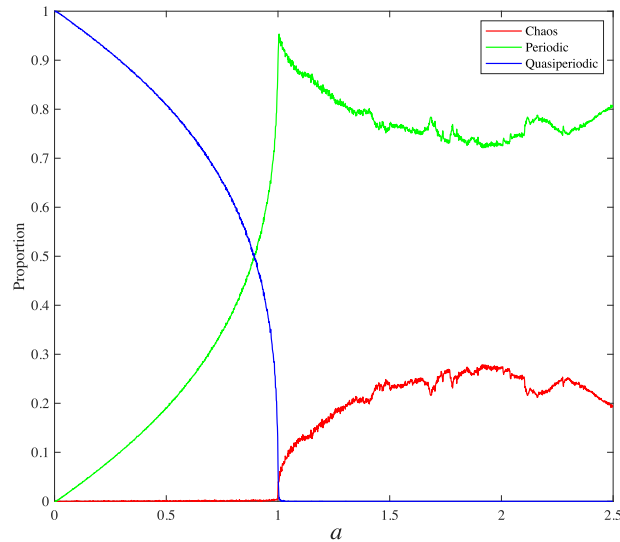


FIG. 3. The proportion of chaotic, periodic, and quasiperiodic orbits in the Arnold circle map as a function of a using the data from Fig. 2. For $a \in (0, 1)$, the quasiperiodic proportion follows the power law (6).

The Arnold map is a homeomorphism when $|a| \leq 1$, in which case—as noted in Sec. II—there are two possibilities: either the map is conjugate to a rigid rotation (4) with irrational ω so that the orbit is quasiperiodic, or every orbit is asymptotic to a periodic orbit and $\omega \in \mathbb{Q}$. In either case, the orbits are not chaotic, and the rotation number (3) is independent of x . For $|a| > 1$, the orbits can be chaotic. We use the WBA, recalled in Appendix A 1, to distinguish between regular and chaotic orbits. In particular, T iterates are used to calculate the approximation ω_T (A8) of the rotation vector (3). Upon T additional iterates, we compute dig_T (A4), an estimate of the precision of ω_T . If the precision is low, $\text{dig}_T < D_T$ (A5), the orbit is classified as chaotic. There have been other studies of chaos in Arnold’s circle map using other means, including lower bounds for the topological entropy^{31,32} and numerical computation of Lyapunov exponents.³³

Here and for the computations discussed below, we chose a grid of $\Omega \in [0, 1]$ that is shifted slightly away from rationals to avoid low-order resonances. Each orbit begins at the same, arbitrary initial point $x(0) = 0.117789164297101$ and is initially iterated 500 times to remove transients. The new initial point $x(500)$ is then iterated with $T = 10^5$ to both compute dig_T and ω_T . A histogram of dig_T from the computation of ω_T is shown in Fig. 1 for three values of a . In each case, there are two well separated peaks in the dig_T distributions, giving a sharp distinction between chaotic and regular orbits.

For example, when $a = 0.8$, where f is a homeomorphism, the average accuracy is $\langle \text{dig}_T \rangle = 15.00$, and the minimum is $\text{dig}_T = 6.76$. Only 0.11% of the orbits have $\text{dig}_T < 9$ and are, thus, incorrectly classified as chaotic. By contrast 35% of the orbits have $\text{dig}_T \geq 16$ —Fig. 1 truncates the accuracy at 16 since the calculations are in double precision. Moreover, this tallest peak is trimmed in the figure to make the portions of the histogram with smaller values of dig_T more visible. When $a > 1$, there is a third small peak in the

TABLE I. Fraction of orbits of Arnold's circle map that have $\text{dig}_T \geq 16$, are chaotic ($\text{dig}_T < 9$), and have rational or irrational rotation number, using 10^4 values of Ω for each a with $T = 10^5$ and (A14). For $a \leq 1$, compare the irrational fraction (column 5) with the power law (5) (last column).

a	$\text{dig}_T \geq 16$	Chaotic	Rational	Irrational	(5)
0.5	0.1986	0.0006	0.1919	0.8075	0.8044
0.8	0.3456	0.0011	0.3917	0.6072	0.6033
0.9	0.4170	0.0009	0.5087	0.4904	0.4853
0.99	0.5974	0.0022	0.7622	0.2356	0.2355
1.0	0.5095	0.0026	0.8813	0.1161	0
1.01	0.5237	0.0580	0.9397	0.0023	
1.02	0.5326	0.0709	0.9282	0.0009	
1.5	0.6524	0.2343	0.7657	0.0000	
2.0	0.6863	0.2711	0.7289	0.0000	

distributions of Fig. 1 near $\text{dig}_T \sim 8.5$; for these orbits, the distinction between regular and chaotic is less clear. The criterion (A6) is conservative in the sense that most of these orbits are taken to be chaotic.

For regular orbits, we use the Farey tree algorithm of Appendix A 2 to effectively separate rotation numbers into rationals and irrationals, thereby distinguishing between periodic and quasiperiodic orbits. This algorithm computes the minimal denominator (A10) and then uses criterion (A15) to designate ω_T as *irrational* or not. We find that when $a = 0.8$, 60.72% of the 10^4 orbits shown in Fig. 1 have effectively irrational rotation numbers while 39.17% are identified as rational (the remaining 0.11% being omitted since these have $\text{dig}_T < 9$). Results of these computations for additional values of a are given in Table I.

It is interesting to note that, for $a = 0.8$, all but 0.9% rotation numbers with the maximum accuracy $\text{dig}_T = 16$, are rational: it is easier to compute an accurate value for the rotation number if the orbit is periodic. On the other hand, 15.7% of the rational rotation numbers do have $9 < \text{dig}_T < 16$.

The classification of orbits with $(\Omega, a) \in [0, 1] \times [0, 2.5]$ for 2000×2000 grid is shown in Fig. 2. When $a < 1$, Fig. 2(a) is consistent with the nonresonant orbits having a nonzero measure, $\mu(a) > 0$. Figueras *et al.*³⁴ used computer assisted proofs to show that

$$0.860748 < \mu(0.25) < 0.914161.$$

Here, the lower bound is based on their a posteriori KAM theorem, and the upper was obtained by excluding tongues for rigorously computed orbits up to period 20. From our computations, $\mu(0.25) = 0.9134$. Their rigorous computations are very time intensive, and it would be impractical to use them to compute anything like the number of parameter values that we have done. Thus, our fast but purely numerical method is a complement to the more time consuming rigorous methods.

Świątek³⁵ has rigorously shown that the tongues have a full measure for $a = 1$, and Khanin³⁶ proved that the Hausdorff dimension of the nonresonant set is then less than one. The computations shown in Table I erroneously predict a small but nonzero fraction of quasiperiodic orbits when $a = 1$, which we attribute to the selected cutoffs in criterion (A15).

The computed proportions of chaotic, resonant, and nonresonant orbits are shown as a function of a in Fig. 3. When $0 < a < 1$, the proportion of nonresonant orbits $\mu(a)$ is close to the previously proposed power law,^{2,3}

$$\mu(a) \simeq (1 - a)^{0.314}. \quad (5)$$

As seen in Table I, the value predicted by (5) is within 0.005 of our computations when $a < 1$. For example, at $a = 0.99$, the Farey algorithm identifies 2356 rotation numbers as “irrational,” which is close to $\mu(0.99) = 0.2355$ from (5). We fit the data in Fig. 3 to the more general form

$$\mu(a) = (1 - a)^{p_1 + p_2(1-a)} \quad (6)$$

using a log-linear least squares fit. This form was selected given the known values $\mu(0) = 1$, and $\mu(1) = 0$, but included a higher order term in the exponent, since there is no theoretical reason why the power law should have only a single term. Our fit gives

$$p_1 = 0.3139 \quad p_2 = -0.0208. \quad (7)$$

The root mean squared (rms) error between the power law and the computed data for $\mu(a)$ (not the log) is 0.0024. By contrast, if we set $p_2 = 0$, the best fit gives $p_1 = 0.3139$ with rms error 0.00449. If we instead compare our data directly with (5), the rms error is 0.00454.

As is well known, the dynamical behavior of the Arnold circle map changes abruptly at $a = 1$. In Fig. 2(b), when $a < 1$, there is only a nearly invisible “dust” of points that are falsely labeled as chaotic—0.07% of the points in this range. For $a > 1$, the fraction of chaotic orbits in Fig. 3 grows but has large fluctuations caused by the well-known bifurcations of the periodic orbits. Conversely, the computed fraction of quasiperiodic orbits for $a > 1$ is essentially zero. Indeed when $a = 1.02$, only 9 of the 10^4 orbits in Table I are mistakenly identified as “irrational” by the Farey algorithm, and by $a = 1.5$, there are no incorrectly identified orbits. This can also be observed in Fig. 2: when $a > 1$, there are no visible points in panel (a) that would correspond to falsely labeled nonresonant orbits; moreover, for $a \in (1.005, 2.5]$, the proportion of orbits measured to be nonresonant is less than 0.55%.

IV. TORUS MAPS

We now consider fully coupled maps on \mathbb{T}^2 using the form (1) with

$$g(x_1, x_2) = \frac{\varepsilon}{2\pi} \begin{pmatrix} a_1 \cos(2\pi(x_1 + \phi_1)) + a_2 \cos(2\pi(x_2 + \phi_2)) \\ a_3 \cos(2\pi(x_1 + \phi_3)) + a_4 \cos(2\pi(x_2 + \phi_4)) \end{pmatrix} \quad (8)$$

Grebogi *et al.*^{4,5} studied similar maps in order to gain an understanding of the typical case, and a number of other specific cases have also been studied.^{29,37–43} For simplicity, we will normalize the amplitudes $a \in \mathbb{R}^4$ so that $\|a\|_1 = 1$; in this case, the strength of the forcing function is governed by the parameter ε , and without loss of generality we take $\varepsilon \geq 0$.

In the one-dimensional case, there were three types of orbits: periodic (ω rational), quasiperiodic (ω irrational), and chaotic orbits. Since the latter does not occur for a diffeomorphism, verification of the power law (6) for Arnold's map when $0 < a < 1$ required only the study of a single class of orbit. In higher dimensions,

quasiperiodic orbits can be either resonant or incommensurate, so there are additional classes of orbits. As in the circle map case, the proportion of incommensurate orbits is one at $\varepsilon = 0$, and—as we will see—there exists a critical value $\varepsilon_{\text{crit}}$ above which there are no incommensurate orbits. Thus, it seems plausible that a power law like (12) could hold for $\varepsilon < \varepsilon_{\text{crit}}$. However, since chaotic orbits can occur even for diffeomorphisms, any test of such a form requires computation of all four classes of dynamical behavior.

In the first part of this section, Sec. IV A, we discuss the classification of rotation vectors, and then in Sec. IV B we obtain the critical value $\varepsilon_{\text{crit}}$ above which the map is guaranteed to not be a homeomorphism. The dynamics are studied in Sec. IV C for a “typical” set of amplitudes and phases in (8). Finally, in Sec. IV D, we study how the proportions of classes of orbit types vary as the amplitudes change and show that there is no universal power law.

A. Resonance and incommensurability

Perhaps, the most natural generalization of the rational vs irrational dichotomy for rotation numbers to higher dimensions is to ask whether a vector has rational components, i.e., $\omega = \frac{p}{q}$ for some $p \in \mathbb{Z}^d$, $q \in \mathbb{N}$. A more general concept, that of *commensurability*, *resonance*, or *mode-locking*, corresponds to the existence of $m \in \mathbb{Z}^d \setminus \{0\}$ and $n \in \mathbb{Z}$ such that

$$\omega \in \mathcal{R}_{m,n} = \{\alpha \in \mathbb{R}^d : m \cdot \alpha = n\}, \quad (9)$$

a codimension-one plane. Such an ω has *resonance order* $M = \|m\|_1$ if this is the smallest length of a (nonzero) vector m for which $\omega \in \mathcal{R}_{m,n}$. The set of vectors that do not lie in any resonant plane are *incommensurate* or *nonresonant*. An example is $\omega = (\sqrt{2}, \sqrt{5})$. When f is conjugate to a rigid rotation (4), these orbits are dense on \mathbb{T}^d .

For $d = 2$, the sets $\mathcal{R}_{m,n}$ are lines; these are shown in Fig. 4 up to order $M = 7$. The *rank* of resonance for a given ω is the number of independent commensurability vectors m ; i.e., the dimension of the smallest affine vector space containing all the lines $\mathcal{R}_{m,n}$ through ω . In the figure, the rank-two frequency vectors are the points at which nonparallel lines intersect. Note that ω is rational only if it has rank two: these correspond to eventually periodic orbits.

Commensurabilities that have lower rank are partially resonant, such as the rank-one vector $\omega = (3\sqrt{2}, 2\sqrt{2} - 1)$, which lies in $\mathcal{R}_{m,n}$ for $m = (2, -3)$ and $n = 3$ so that $M = 5$. A rank-one ω corresponds to a *resonant orbit*, for $d = 2$ these are typically asymptotic to invariant circles.

The above discussion gives rise to a numerical method for classifying dynamics. Each orbit is labeled chaotic or regular using the methods in Appendix A 1 and criterion (A7). Given the accurately approximated ω_T for a regular orbit, Appendix B gives a numerical method for distinguishing between the three commensurabilities. Nonresonant (rank-zero resonant) points, with an incommensurate rotation vector, are found using criterion (A20). Periodic points (rank-two resonant) are found using criterion (A21), and resonant (rank-one resonant) points are given by criterion (A22).

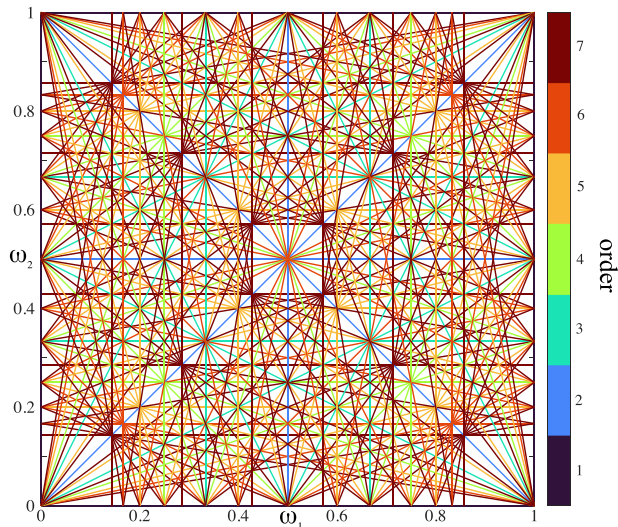


FIG. 4. Resonance lines up to order $\|m\|_1 = 7$.

B. Critical parameter

In this section, we establish the existence of a critical amplitude, $\varepsilon_{\text{crit}}$, so that the map (1) with (8) cannot be conjugated to a rigid rotation for $\varepsilon > \varepsilon_{\text{crit}}$: it fails Lemma 1. The experience with circle maps indicates that local invertibility should be important dynamically. Note, however, that even when $0 \leq \varepsilon < \varepsilon_{\text{crit}}$, where local invertibility holds, this lemma does not guarantee the existence of a conjugacy nor the absence of chaotic orbits.

Recall from Lemma 1 that a necessary condition for the map (1) with (8) to be diffeomorphic to rigid rotation is that it has a nonsingular Jacobian,

$$\det(Df) = \det(I + \varepsilon H) = \varepsilon^2 \det H + \varepsilon \operatorname{tr} H + 1, \quad (10)$$

$$\varepsilon H \equiv Dg = -\varepsilon \begin{pmatrix} a_1 \sin(2\pi(x_1 + \phi_1)) & a_2 \sin(2\pi(x_2 + \phi_2)) \\ a_3 \sin(2\pi(x_1 + \phi_3)) & a_4 \sin(2\pi(x_2 + \phi_4)) \end{pmatrix}.$$

To be nonsingular, $\det(Df)$ must be nonzero for all $(x_1, x_2) \in \mathbb{T}^2$; therefore, we define the critical value of ε as

$$\varepsilon_{\text{crit}} \equiv \min \left\{ \varepsilon \geq 0 : \min_{x \in \mathbb{T}^2} (\det(Df)) \leq 0 \right\}, \quad (11)$$

i.e., the smallest positive ε for which $\det(Df) = 0$ for some value of x . When $\varepsilon > \varepsilon_{\text{crit}}$, conjugacy to rigid rotation is not possible. Since $Df = I$ when $\varepsilon = 0$, we know that—if it exists— $\varepsilon_{\text{crit}} > 0$. In order to compare behavior for different nonlinearities in Sec. IV D, we will find that it is appropriate to scale with respect to $\varepsilon_{\text{crit}}$.

We claim that if $\det H$ is not identically zero, there is some $x \in \mathbb{T}^2$ such that $\det H < 0$. For example, suppose for simplicity that $\phi_i = 0$, $i = 1, \dots, 4$ in (10). In this case, since sine is an odd function, if $\det(H(x_1, x_2)) > 0$, then $\det(H(-x_1, x_2)) < 0$. In turn, (10) then implies that, if ε is sufficiently large, $\det(Df(-x_1, x_2)) < 0$; therefore, $\varepsilon_{\text{crit}}$ exists. By a similar argument in Appendix B, we show that this

result holds for all phases and amplitudes except for the trivial case $a_1 = a_4 = 0$ and $a_2 a_3 = 0$.

We find (11) numerically using standard root finding methods. For example, for the coefficients of *case (0)*, given in Table III of Appendix C, we find

$$\varepsilon_{\text{crit}} = 2.220\ 44.$$

The existence or nonexistence of a conjugacy to rigid rotation will not only depend upon ε , but also upon Ω , and of course the resulting ω . Moreover, as we see below, even when $\varepsilon < \varepsilon_{\text{crit}}$, chaotic orbits can occur.

C. A “typical” case

In this section, we study the dynamics for a fixed set of parameters a and ϕ as a function of ε and Ω [see “*case (0)*” in Table III of Appendix C]. The goal is to see “typical” behavior (as much as one can with a limited set of examples). While no single parameter set will give all possible dynamics, for *case (0)* the amplitudes a_i have comparable sizes, and the phases ϕ_i are at least not close to rationals with small denominators. We feel it is useful to look at a single case in detail before giving comparisons between a larger set of cases in Sec. IV D.

Six typical phase portraits are shown in Fig. 5 for the values of ε and Ω listed in Table II. For the first three panels, $\varepsilon = 0.8$. Panels (a) and (c) show nonresonant orbits that appear to be dense on \mathbb{T}^2 and for which the rotation vectors, given in Table II, are incommensurate according to criterion (A20). Panel (b) shows a resonant orbit with the low-order resonance $(m, n) = (1, -1, 0)$; the orbit lies on an attracting circle that wraps once around both horizontally and vertically. In panel (d), where $\varepsilon = 1.5$, the orbit is resonant with $m = (2, 7, 6)$, as indicated by the fact that the invariant circle wraps seven times horizontally and twice vertically. Of course, there are also parameters for which the attractor is periodic for this family of maps, but due to their simplicity, we did not opt to depict any here. Panels (e) and (f) show examples that imply criterion (A7) is chaotic. Visually (f) appears to be more chaotic than (e), and a check of the two Lyapunov exponents supports this: for $T = 10^6$, $\lambda = \{0.0256, -0.0644\}$ for (e) and $\lambda = \{0.2892, -0.0639\}$ for (f). Though (e) has a positive exponent it seems quite close to the “weak chaos” seen for quasiperiodically forced circle maps with strange non-chaotic attractors (SNAs). We use the WBA to study such systems in a separate paper.⁴⁴

The proportions of the four types of orbits, distinguished using the methods discussed in Appendix A, are shown in Fig. 6 as a function of ε for *case (0)*. Here we use a grid of 402 evenly spaced

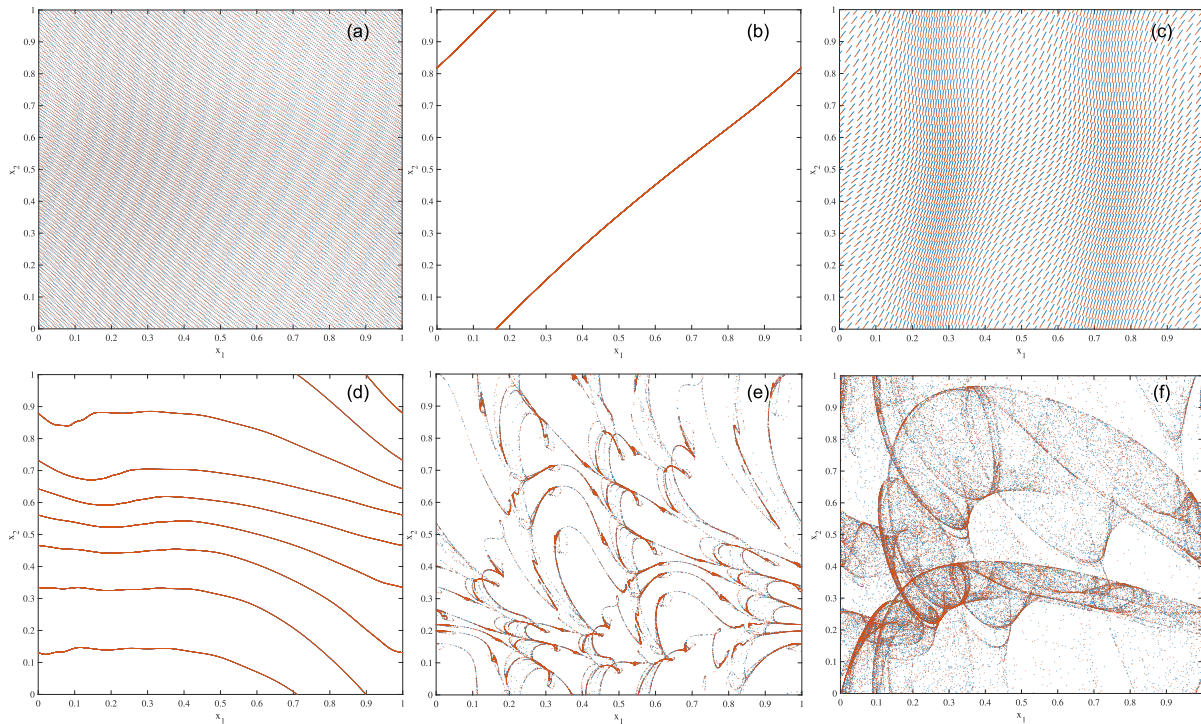


FIG. 5. Orbits of (1) on \mathbb{T}^2 with g given by (8). Each panel shows $3(10)^4$ iterates for two initial conditions (red and blue), with transients removed. The amplitudes and phases correspond to *case (0)* in Table III, and values of ε , Ω , the computed ω_T and dig_T are given in Table II. (a) Two-torus; (b) resonant circle with $(m, n) = (1, -1, 0)$; (c) two-torus; (d) resonant circle with $(m, n) = (2, 7, 6)$; (e,f) chaotic trajectories when the map is noninvertible. Using $T = 10^6$ for the WBA gives $\text{dig}_T > 12$ for the regular orbits in panels (a)–(d); for the chaotic orbits (e) $\text{dig}_T = 4.05$ and (f) $\text{dig}_T = 2.55$.

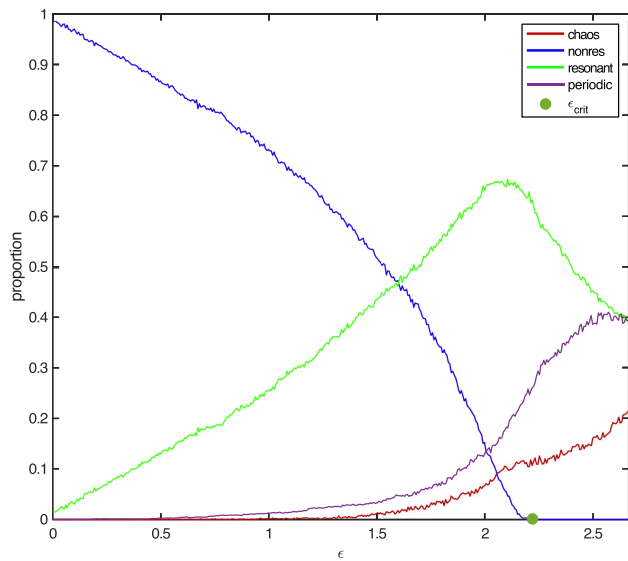


FIG. 6. The proportion of resonant, nonresonant, periodic, and chaotic orbits in the 2D Arnold map. The green dot on the ϵ -axis shows the point $\epsilon_{\text{crit}} \approx 2.22044$ at which the map first becomes locally noninvertible. As in the 1D case, there are no nonresonant orbits for $\epsilon > \epsilon_{\text{crit}}$.

$\epsilon \in [0, 1.2\epsilon_{\text{crit}}]$ and the same set of 2500 randomly chosen $\Omega \in [0, 1]^2$ for each ϵ . Much of the behavior is similar to the 1D case of Sec. III. By Lemma 1, the proportion of nonresonant orbits is zero for $\epsilon > \epsilon_{\text{crit}}$ (the green dot on the ϵ -axis in the figure), and indeed we observe that near this point the computed proportion (blue curve) does reach zero. However, unlike the 1D case, this proportion appears to approach zero at ϵ_{crit} with zero slope. Moreover, Fig. 6 indicates that chaotic orbits (red curve) occur for $\epsilon < \epsilon_{\text{crit}}$. A similar result, using Lyapunov exponents, was obtained by Yamagishi and Kaneko⁴⁵ for high-dimensional torus maps.

We observe that resonant proportion (green curve) peaks just below ϵ_{crit} . The proportion of periodic orbits (purple curve) also reaches a maximum but now near $\epsilon = 2.5$, beyond the resonant peak. Both the periodic and chaotic proportions grow more-or-less monotonically as ϵ crosses ϵ_{crit} .

Orbit-type statistics like those shown in Fig. 6 were found in the work of Grebogi *et al.*⁴⁵ who studied torus maps for $d = 2$ and 3. In particular, they considered a finite Fourier series for the function g in (1) and—for randomly chosen amplitudes and phases—computed the fractions of the attractors that are m -tori for $m \in \{0, 1, \dots, d\}$, and the fraction that was chaotic. To do this, they computed the Lyapunov spectrum $(\lambda_1, \lambda_2, \dots, \lambda_d)$. If all $\lambda_i = 0$, the orbit was classified as lying on a d -torus; if all exponents were nonpositive, and m were zero, the orbit should lie on an m -torus. Finally, if there were any positive exponents, the attractor was classified as chaotic. Yamagishi and Kaneko⁴⁵ also used the Lyapunov spectrum to classify dynamics of torus maps with $d \sim 100$. These studies suffer from the problem that accurate computation of the Lyapunov spectrum is difficult.

While Fig. 6 gives a large amount of information on the behavior of orbits aggregated over the range $\Omega \in [0, 1]^2$, it does not show

how these are organized as Ω varies. Even when a and ϕ are fixed, it would be difficult in a single graph to visualize the categories of orbits for each Ω and ϵ . We show slices through these data for fixed ϵ in Fig. 7. Here the computed ω_T is shown for nonresonant (top) and resonant and periodic (bottom) orbits for $\epsilon = 1.9$ (left), 2.0 (middle), and 2.1 (right). The nonresonant panels show empty strips along resonance lines, recall Fig. 4, and holes surrounding the rank-two resonances; these correspond to the Arnold tongues surrounding periodic orbits. Kim *et al.*^{29,46} studied the formation of Arnold tongues for a similar torus map using the bifurcation theory. They noted that the region in (Ω_1, Ω_2) for which there exists a periodic attractor (a “resonance region”) that need not be simply connected and that the number of periodic orbits with a given rational rotation vector $\omega = (p_1, p_2)/q$ can vary.

To gain further information about the role of Ω , Fig. 8 shows ω_T for resonant (green) and nonresonant (blue) orbits with fixed $\Omega_2 = \gamma = (\sqrt{5} - 1)/2$, the golden mean. This corresponds to a slice through Fig. 7 with fixed Ω_2 ; however, now ϵ varies over $[0, \epsilon_{\text{crit}}]$. This Ω slice avoids the larger gaps due to lower-order resonance tongues around the periodic orbits in Fig. 7. Panel (a) is a projection onto the $\omega_T = (\omega_1, \omega_2)$ plane, showing how these vary as ϵ grows. Panel (b) shows the same data, but this time in $(\omega_1, \omega_2, \epsilon)$; this is a vector-valued version of a devil’s staircase of resonant and incommensurate rotation vectors.

D. Varying the amplitudes

We now proceed to consider more general amplitudes a and phases ϕ for (8) using eight parameter sets given in Table III of Appendix C. The first four sets are chosen randomly, but the last four are chosen to illustrate noteworthy dynamical categories. In each case, we normalize $\|a\|_1 = 1$ and compute ϵ_{crit} using (11)—this is given in the last column in Table III. The four panels of Fig. 9 show the proportion of (a) nonresonant, (b) resonant, (c) periodic, and (d) chaotic orbits for the eight parameter sets as a function of ϵ , scaled by ϵ_{crit} . One can see immediately from Fig. 9 that *case* (4) (purple) and *case* (7) (orange) are outliers. These correspond to uncoupled and semidirect cases and will be discussed further below.

Panel (a) shows that in each of the eight cases the proportion of nonresonant orbits drops to zero at $\epsilon/\epsilon_{\text{crit}} = 1$. These curves illustrate that there is no universal power law for the nonresonant orbits of the form

$$\mu(\epsilon) \simeq \left(1 - \frac{\epsilon}{\epsilon_{\text{crit}}}\right)^p \quad (12)$$

that would be analogous to (5), since the curves have different shapes. Indeed, since some of the curves [e.g., *cases* (3), (5), and (6)] appear to have zero slope at both $\epsilon = 0$ and ϵ_{crit} , they cannot not satisfy a single power law on the full range $[0, \epsilon_{\text{crit}}]$. Even if the form (12) was valid asymptotically close to ϵ_{crit} , p would need to be greater than one for the fully coupled cases, in stark contrast to (5).

Most of the resonant proportions, shown in Fig. 9(b), exhibit smooth peaks for some $\epsilon < \epsilon_{\text{crit}}$. The outliers are again *cases* (4) and (7), where there are sharp peaks at ϵ_{crit} . The periodic orbit proportions peak as well, but not at the same ϵ as the resonant peaks [and in *case* (7) there are no periodic orbits]. Panel (d) shows that

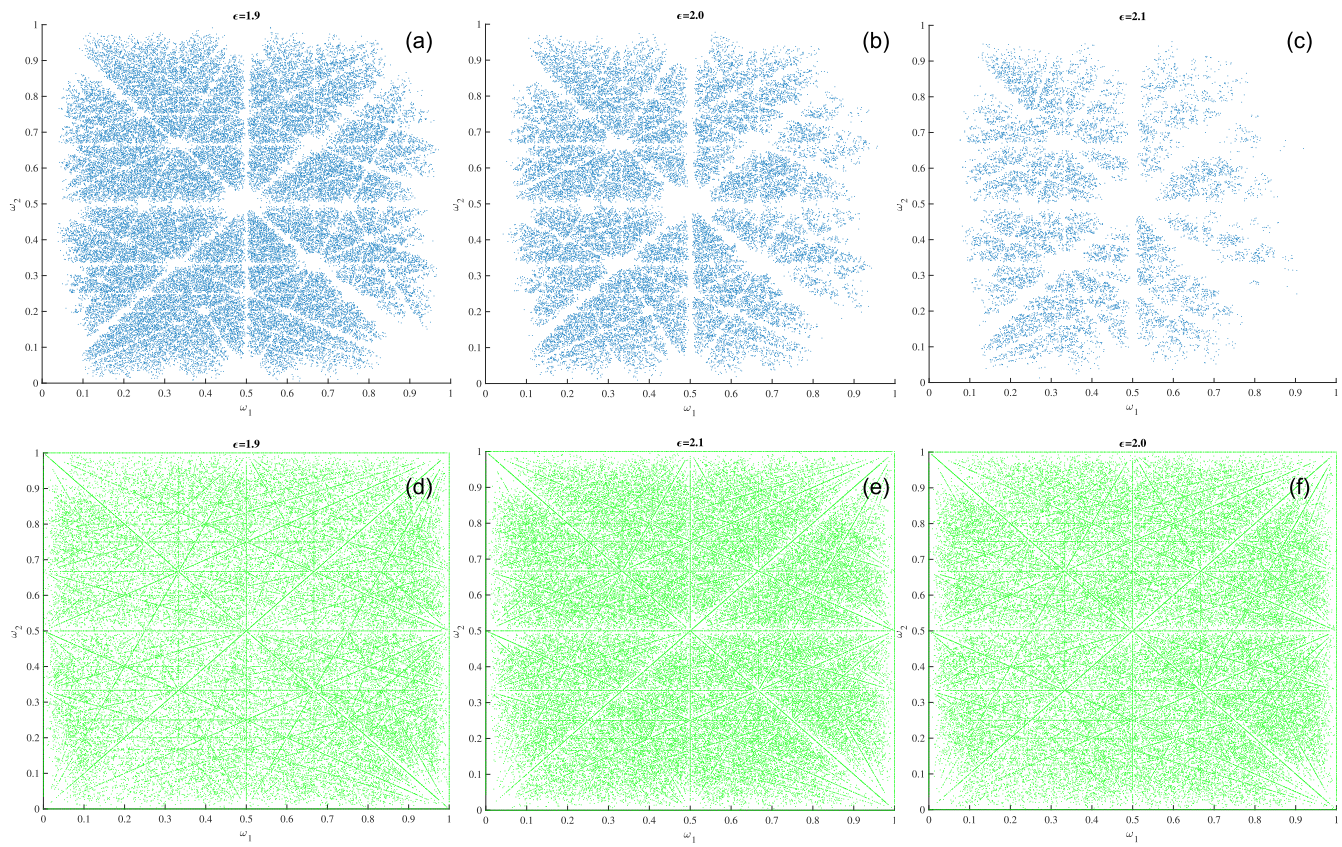


FIG. 7. The rotation numbers $\omega_T = (\omega_1, \omega_2)$ of the nonresonant (top) and resonant/periodic (bottom) orbits for case (0) in Table III and 250 000 $\Omega \in [0, 1]^2$, with $\varepsilon = 1.9$ (left), 2.0 (middle), and 2.1 (right). As ε approaches $\varepsilon_{\text{crit}}$, the nonresonant set becomes more sparse, and the gaps near the lower order resonance lines and periodic points widen.

21 January 2025 19:23:49

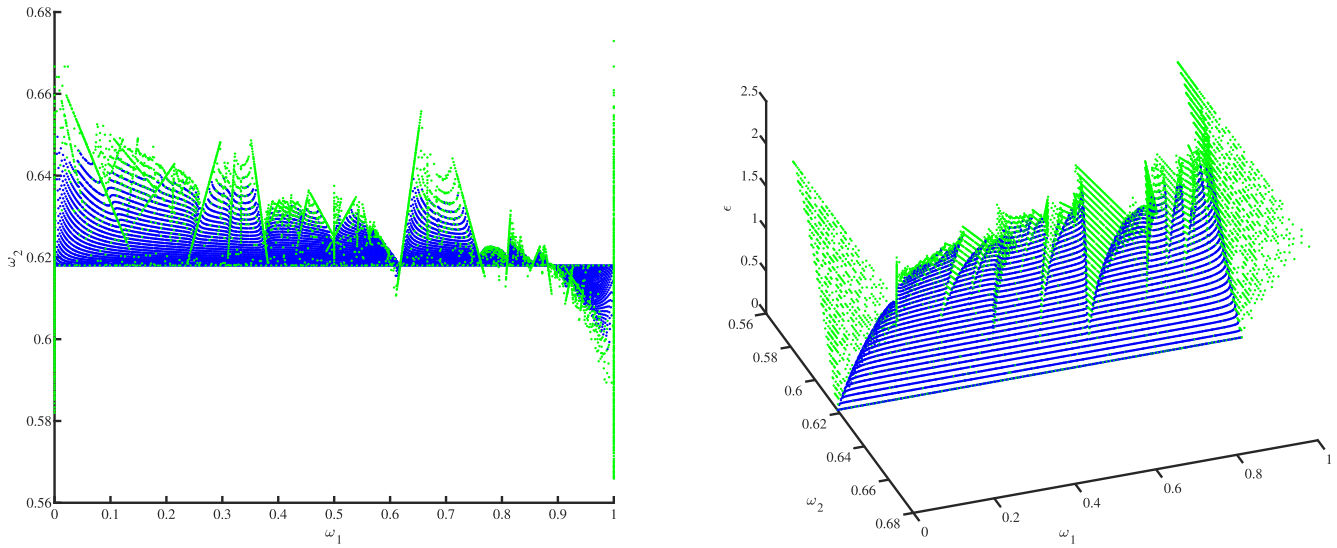


FIG. 8. (a) Resonant (green) and nonresonant (blue) orbits for $\Omega_1 \in [0, 1]$ with $\Omega_2 = \gamma$ and 30 evenly spaced values of $\varepsilon \in [0, \varepsilon_{\text{crit}}]$ showing ω_T for $T = 10^6$. (b) A 3D view of the data in (a) for coordinates $(\omega_1, \omega_2, \varepsilon)$.

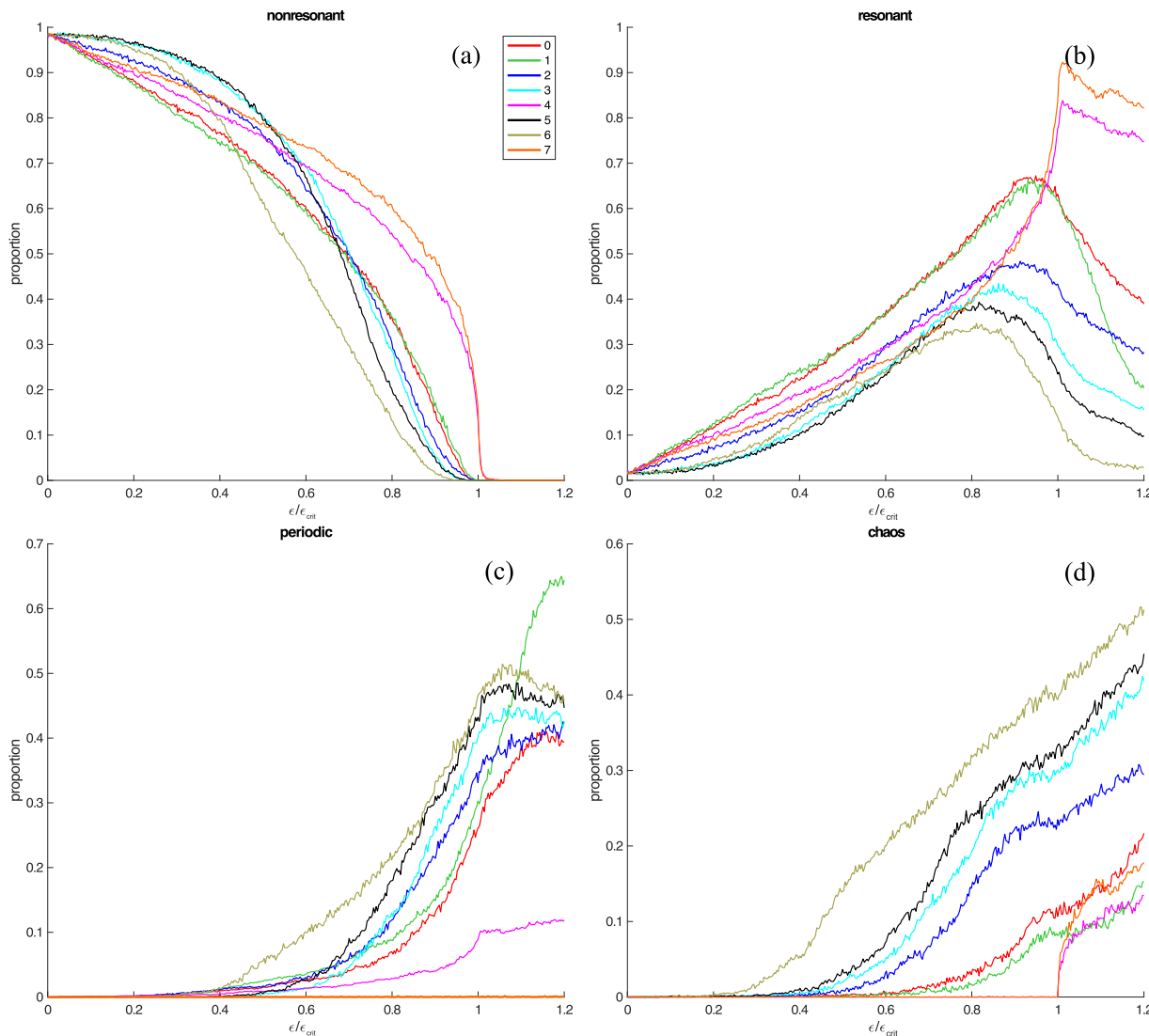


FIG. 9. The proportion of (a) nonresonant, (b) resonant, (c) periodic, and (d) chaotic orbits as a function of $\epsilon/\epsilon_{\text{crit}}$ for the eight sets of the coupling and phase parameters a and ϕ in Table III. Note that the vertical scales vary for the panels.

the onset of chaos is considerably below ϵ_{crit} , again with the exception of cases (4) and (7). All of these observations are consistent with those for other randomly chosen a and ϕ that we considered, but that are not shown.

We now consider four special subcategories, describing their distinct behaviors. Though these are extreme examples, we have observed that for nearby amplitudes, the behavior is similar. Though we have not systematically varied the phases, these do not seem to change the qualitative behavior.

- *Uncoupled components:* If $a = (1, 0, 0, 0)$, the system is uncoupled and essentially 1D, the second component $\omega_2 = \Omega_2$ will be

irrational for almost all Ω . Thus, the rotation vector is incommensurate depending only on the first component which is the Arnold circle map. Therefore, the power law (12) will hold with the 1D value $p_1 \approx 0.3139$ from (6). Of course, the same considerations apply to the case $a = (0, 0, 0, 1)$.

More generally, the uncoupled case corresponds to $a = (1 - u, 0, 0, u)$, and we can restrict to $u \in [0, \frac{1}{2}]$ by symmetry. Since $u \leq \frac{1}{2}$, $\epsilon_{\text{crit}} = (1 - u)^{-1}$ where the first component becomes noninvertible. An example is case (4) where $u \approx 0.24$. Figure 9 shows that orbit type proportions for this case have shapes similar to those for Arnold's map in Fig. 3. In particular, there is no chaos for $\epsilon < \epsilon_{\text{crit}}$. Note that the rank-two

resonances, panel (c), correspond to the cross product of Arnold tongues for each of the decoupled 1D maps; there is no analog of this in Fig. 3.

For this uncoupled case, the proportion of orbits with irrational ω_1 and that with irrational ω_2 will both satisfy (12) but the effective critical parameters will be different, $\varepsilon_{\text{crit}} = (1-u)^{-1}$ and u^{-1} , respectively. However, the incommensurate proportion for the 2D rotation vector ω can have a different behavior. The simplest case, $u = \frac{1}{2}$, has $\varepsilon_{\text{crit}} = 2$ and would have a non-resonant proportion μ that is approximately the square of the proportions for each 1D map; therefore, we expect (12) to hold with $p \approx 2p_1$. However, note that this does not take into account rational relations like (9) with both m_1 and $m_2 \neq 0$. By contrast, if u is small, the second map will have an irrational proportion that is near 1 and changes only slightly as ε grows to $\varepsilon_{\text{crit}} = (1-u)^{-1}$. This should give (12) with $p \approx p_1$, close to the 1D case. More generally, we observe that the power p varies continuously between p_1 and $2p_1$ as u grows from 0 to $\frac{1}{2}$.

We have also looked at weakly coupled examples (not shown); these show orbit-type proportions similar to case (4).

- *Semidirect product:* When $a = (0, u, 0, 1-u)$, the behavior is similar to the 1D case even for nonzero u since the map is a semidirect product. [Of course, the case $(1-u, 0, u, 0)$ is of this type as well.] An example is *case* (7) where $a \approx (0, 0.35, 0, 0.65)$. Here, the second component is Arnold's circle map and the first is linear but driven by the dynamics of x_2 . Thus, this case is also essentially 1D and $\varepsilon_{\text{crit}} = (1-u)^{-1}$. Since $a_1 = 0$, we might expect that $\omega_1 = \Omega_1$, at least for $\varepsilon < \varepsilon_{\text{crit}}$ where the dynamics of x_2 is either conjugate to an irrational rotation or asymptotically periodic. Note that there are no periodic orbits in panel (c) for this case because the grid of Ω values was chosen to avoid the rationals.

case (6) is a weakly coupled perturbation of the trivial semidirect case with $u \approx 1$. This case is also near the anti-coupled case discussed below.

- *Quasiperiodic forcing:* When $a = (1-u, u, 0, 0)$, the first component is generically quasiperiodically forced. We consider this class of maps separately in a forthcoming paper.⁴⁴ For fixed $\Omega_2 = \gamma$, the proportion of nonresonant orbits appears to have zero slope at $\varepsilon_{\text{crit}}$ and, thus, does not satisfy a power law with $0 < p < 1$. This also persists when we allowed Ω_2 to vary. Equivalent behavior occurs for $(0, 0, u, 1-u)$.
- *Anti-coupled system:* When $a = (0, 1-u, u, 0)$, the dynamics is fully 2D, but could be thought of as anti-coupled. For this case, $\varepsilon_{\text{crit}} = (u(1-u))^{-1/2}$. An example is *case* (5) (black) in Fig. 9 where $u \approx 0.23$. Here, we again find that the proportion of nonresonant orbits has zero slope $\varepsilon = \varepsilon_{\text{crit}}$, with the fastest decay when $u \approx 0$ or (by symmetry) $u \approx 1$. We suspect that this is due to the larger fraction of chaotic orbits at smaller $\varepsilon/\varepsilon_{\text{crit}}$. Note that *case* (3) is a slightly perturbed anti-coupled system, and its proportion curves are close to *case* (5) even though the effective value of u is different. As mentioned above, *case* (6) can also be thought of as a perturbation of a trivial version of this case with $u = 0$. Baesens *et al.*³⁹ previously studied mode locking for an anti-coupled case with $u = \frac{1}{2}$.

V. CONCLUSIONS AND FUTURE DIRECTIONS

In this paper, we have used efficient techniques to characterize the dynamics of orbits of one- and two-dimensional torus maps, which are homotopic to the identity. We used the convergence rate of the WBA to distinguish between chaotic and regular orbits, defining a threshold for the precision, dig_T (A4), after a fixed number of iterates T . Given an accurate value for rotation vector ω_T , we determined if the vector is nearly resonant by finding the smallest order of a resonance vector within a distance δ . This allows us to characterize regular orbits as incommensurate (nonresonant), rank-one (resonant), or rank-two (periodic). This computation is especially efficient for the 1D case, where we can use the Farey tree to compute the minimum denominator (A10).⁹ We hope in the future that an efficient algorithm to compute (A18) for the 2D case can be found. Meanwhile, we used a brute force method, following our previous work on volume-preserving maps.¹⁰

Our methods naturally extend to higher dimensional maps. However, there are some significant computational challenges for $d > 2$. The WBA method extends without any difficulty to three and higher dimensions;¹⁰ other than the standard problem of needing more initial conditions and iterates to get a sense of the full dynamics, there are no difficulties to distinguish between chaotic and regular orbits. Finding periodic (ie. rank- d resonant) orbits in dimension d is also just a matter of checking that the rotation vector is rational in each component.

However, there are computational issues that may limit our ability to distinguish lower rank resonances. In Appendix A, we observed that for random values in \mathbb{T}^1 the typical denominator of δ -close rational approximation to an irrational scales as $q_{\min} \sim \delta^{-1/2}$, recall (A11). Of course, q_{\min} is the 1D version of the resonance order M , (A18). In dimension two, for random values in \mathbb{T}^2 , we observed that M scales as $M \sim \delta^{-1/3}$, recall (A19). There is theoretical support for the $d = 1$ result⁴⁷ and Marklof^{48,49} has shown that for the general d -dimensional case (A19) becomes

$$\langle \log_{10}(M(\omega, \delta)) \rangle \approx -\frac{1}{d+1} \log_{10} \delta + c_d. \quad (13)$$

This is a new torment to add to the usual “curse of dimensionality.” As d grows, the typical resonance order of a theoretically incommensurate vector will be pushed closer to zero for a given precision δ . For example, if for $d = 4$ we were to use the same precision, $\delta = 10^{-9}$, that we used in the current paper, then the typical resonance order would be $M \sim 10^{9/5} \sim 63$. Therefore, the computed order of an incommensurate ω would be small enough that it would be quite hard to distinguish it from a vector that is actually resonant with even the modest resonance order. In order to be able to distinguish these values, one would need the added computational expense of extended precision; moreover, the computation of a frequency ω to higher accuracy would also require increasing the number of iterates T . The calculations would quickly become very slow. We hope that further research in this area will prove us to be overly pessimistic.

ACKNOWLEDGMENTS

Thank you to the referee for their helpful comments. E.S. was supported in part by the Simons Foundation under Award

No. 636383. J.D.M. was supported in part by the Simons Foundation under Award No. 601972. Useful conversations with Nathan Duignan are gratefully acknowledged.

AUTHOR DECLARATIONS

Conflict of Interest

The authors have no conflicts to disclose.

Author Contributions

E. Sander: Conceptualization (equal); Formal analysis (equal); Methodology (equal); Visualization (equal); Writing – original draft (equal); Writing – review & editing (equal). **J. D. Meiss:** Conceptualization (equal); Formal analysis (equal); Methodology (equal); Visualization (equal); Writing – original draft (equal); Writing – review & editing (equal).

DATA AVAILABILITY

The data that support the findings of this study are available from the corresponding author upon reasonable request.

APPENDIX A: COMPUTATIONAL METHODS

In this section, we describe the numerical methods used in Secs. III–IV. We use the weighted Birkhoff average, Appendix A 1, for computing rotation number and identifying chaos. The Farey tree method in Appendix A 2 distinguishes regular orbits that are periodic from those that are quasiperiodic for $d = 1$. The method of resonance orders in Appendix A 3 extends this to higher dimensions to distinguish the resonant (lower-dimensional) invariant tori from those that are nonresonant (full-dimensional).

1. Regularity vs chaos: Weighted Birkhoff averages

We briefly review here the weighted Birkhoff average^{6–8} and how it distinguishes between regular and chaotic orbits.⁹ Given a map $f: M \rightarrow M$, recall that the time average of a function $h: M \rightarrow \mathbb{R}$ along an orbit of f is simply

$$B(h)(z) = \lim_{T \rightarrow \infty} \frac{1}{T} \sum_{t=0}^{T-1} h \circ f^t(z), \quad (\text{A1})$$

if this limit exists. The classic theorem of Birkhoff implies that if the orbit of f is ergodic on a set with invariant measure μ , and if $h \in L^1(M, \mathbb{R})$, then

$$B(h)(z) = \langle h \rangle = \int_M h d\mu$$

for μ -almost every z . However, the convergence to this limit is at best as $1/T$ and can be arbitrarily slow.^{50,51}

To compute the average efficiently and accurately for a length- T segment of an orbit, we modify (A1) using the C^∞ weight function

$$\Psi(s) \equiv \begin{cases} e^{-[s(1-s)]^{-1}} & s \in (0, 1), \\ 0 & s \leq 0 \text{ or } s \geq 1. \end{cases}$$

This exponential bump function limits to zero with infinite smoothness at 0 and 1, i.e., $\Psi^{(k)}(0) = \Psi^{(k)}(1) = 0$ for all $k \in \mathbb{N}$. The

finite-time weighted Birkhoff average (WBA) is then defined by

$$WB_T(h)(z) = \frac{1}{S} \sum_{t=0}^{T-1} \Psi\left(\frac{t}{T}\right) h \circ f^t(z), \quad (\text{A2})$$

with the normalization constant

$$S \equiv \sum_{t=0}^{T-1} \Psi\left(\frac{t}{T}\right). \quad (\text{A3})$$

Das *et al.*⁶ have shown that this gives the same answer as $T \rightarrow \infty$ as (A1); however, for regular orbits (A2) can converge much more quickly. In particular, if the orbit is conjugated to a rigid rotation (4) with a Diophantine rotation vector ω and the map f and function h are C^∞ , then (A2) converges faster than any power,¹²

$$|WB_T(h) - \langle h \rangle| < \frac{C_k}{T^k}, \quad \forall k \in \mathbb{N}.$$

Note that the function Ψ is not the only C^∞ weighting function with these excellent convergence properties. The recent work of Ruth and Bindel⁵² uses reduced rank extrapolation to optimize the choice of weighting function.

We estimate the error of the WBA for a given function h and a given time T by computing the effective number of digits of accuracy,

$$\text{dig}_T = -\log_{10} |WB_T(h)(z) - WB_T(h)(f^T(z))|, \quad (\text{A4})$$

i.e., comparing the result for the first T iterates with that for the next T iterates.^{9,10}

To obtain a criterion distinguishing chaotic and regular orbits, we need to make a choice of cutoff value for dig_T , declaring that orbits with

$$\text{dig}_T < D_T \Rightarrow \text{"chaotic."} \quad (\text{A5})$$

Conversely, all orbits with $\text{dig}_T \geq D_T$ are “nonchaotic.” Based on Fig. 1 for the 1D case, we choose the cutoff,

$$T = 10^5, \quad D_T = 9 \quad (\text{circle maps}). \quad (\text{A6})$$

This guarantees at least nine digits of accuracy in the computed rotation number. For the Arnold circle map in Sec. III, we know that there are no chaotic orbits for $0 < a \leq 1$; with the adopted criterion, our computations falsely identify only 0.07% (1145 out of 1.6×10^6) of the orbits in this range to be chaotic.

For the 2D maps in Sec. IV, we use the criterion

$$T = 10^6, \quad D_T = 9 \quad (\text{two-torus maps}). \quad (\text{A7})$$

Like the one-dimensional case, this is conservative in that chaotic orbits are quite unlikely to be identified as regular.

2. Rational vs irrational: Farey trees

In addition to providing the distinction between regular and chaotic orbits, the WBA can be used to compute an accurate value of the time average of a function h . In particular, we can compute the rotation vector (3) of an orbit for a torus map of the form (1)

using

$$\omega_T = WB_T(F(x) - x) = \Omega + WB_T(g(x; a)). \quad (\text{A8})$$

If T is large enough and the rotation vector exists, we expect $\omega_T \approx \omega(x, f)$ (3). We note that this is by no means the only possible useful h to choose. For example, for quasiperiodic orbits, another choice of h allows one to compute the conjugacy between the map and a rigid rotation.^{6,24}

In this section, we focus on circle maps, $d = 1$, and review the Farey tree method which we developed in a previous paper.⁹ This method, combined with (A8), allows us to distinguish orbits that are periodic—those with rational ω —from those that are dense on a circle with irrational ω .

Even though a numerical determination of the irrationality of ω_T is impossible, we will declare it to be “effectively rational” if it is sufficiently close to a low-order $\frac{p}{q} \in \mathbb{Q}$, i.e., one with a “small” denominator q . A rational is δ -close to x if it lies in the interval

$$B_\delta(x) \equiv (x - \delta, x + \delta). \quad (\text{A9})$$

The smallest denominator of a rational approximation within δ of ω is then

$$q_{\min}(\omega, \delta) \equiv \min \left\{ q \in \mathbb{N} : \frac{p}{q} \in B_\delta(\omega), p \in \mathbb{Z} \right\}. \quad (\text{A10})$$

We previously discussed an efficient method to compute (A10) that uses the Farey tree expansion of ω .⁹ The Farey (or Stern–Brocot) tree computes a sequence of rational approximations that converge to ω . We proved that the first such rational on the tree that falls in $B_\delta(\omega)$ gives q_{\min} .⁹ For example,

$$q_{\min}(\sqrt{2}, 10^{-9}) = 33461$$

(with corresponding numerator $p = 47321$). Note that $q_{\min} \sim 10^{4.52}$, which is close to $\frac{1}{\sqrt{\delta}} = 10^{4.5}$ —as we see next, this is not unusual.

To decide what it means for a denominator to be “small,” we computed q_{\min} for a uniform distribution $\omega \in (0, 1)$; since irrationals have measure one, we take the computed distribution to be that of irrationals. Numerically, we found that the resulting log-denominators have a distribution that is nearly symmetric about the mean

$$\langle \log_{10} q_{\min} \rangle = -\frac{1}{2} \log_{10} \delta + \alpha, \quad (\text{A11})$$

where $\alpha = -0.05 \pm 0.001$, with standard deviation

$$\sigma = 0.2935 \pm 0.0006, \quad (\text{A12})$$

which is independent of δ . In support of this, in a recent paper, Chen and Haynes⁴⁷ proved that as $\delta \rightarrow 0$, $\log_{10} \langle q_{\min} \rangle$ has the form (A11) with a different α . However, this result is for the log of the mean, whereas our numerics were for the mean of the log. More recently, Marklof⁴⁹ has fully verified (A11), showing that $\alpha = -0.0502959\dots$ and $\sigma = 0.293336\dots$, consistent with our numerical results.

It is important to note that it is not just small q_{\min} that correspond to a nearby rational: if an interval $B_\delta(\omega)$ is close to a low-order rational, but does not include this point, then q_{\min} can be much larger than the mean indicated by (A11). For example, if ω is very

close to $\frac{0}{1}$, but δ is so small that $0 \notin B_\delta(\omega)$, then the denominator can be unusually large; for example,

$$q_{\min}(\sqrt{2} \times 10^{-8}, 10^{-9}) = 66040883 \sim 10^{7.8},$$

which is 11σ above the mean (A11). Thus, we will declare a number effectively irrational only if q_{\min} is close to the mean (A11) in the sense of the standard deviation σ . Such an ω is “typical” in the sense of the uniform distribution and, thus, is “irrational.”

For a given accuracy δ , we declare that ω is an approximation of an irrational if

$$\left| \log_{10}(q_{\min}(\omega, \delta)) + \frac{1}{2} \log_{10}(\delta) \right| < s, \quad (\text{A13})$$

for a given tolerance s . We typically choose

$$\delta = 10^{-9} \quad \text{and} \quad s = 1.6875 \approx 5.75\sigma. \quad (\text{A14})$$

This means that we declare that ω approximates an irrational for periods

$$649 < q_{\min} < 1.54(10)^6 \Rightarrow \text{“irrational.”} \quad (\text{A15})$$

This choice of tolerance s means we are quite conservative in designating a rotation number as rational. Using criterion (A14), we incorrectly identify 0.05% of the random ω as rational (since rationals have measure zero, the result should be zero). Similarly, we see in Sec. III that (A14) erroneously identifies only 0.08% of the non-chaotic orbits of the Arnold circle map as having irrational rotation number when $a \in (1, 2.5)$, where it is known that there are no such orbits.

3. Resonant vs incommensurate: Resonance orders

Here, we recall a numerical method that generalizes the Farey tree method of Appendix A 2 to higher dimensions. In particular, given ω_T we wish to compute the rank and resonance order, recall Sec. IV A.

A vector ω is approximately commensurate if $|m \cdot \omega - n|$ is small. In Meiss and Sander,¹⁰ we developed a method for computing such commensurabilities. We say that a vector ω is (m, n) -resonant to precision δ if the resonant plane (9) intersects the ball (A9) about ω ,

$$\mathcal{R}_{m,n} \cap B_\delta(\omega) \neq \emptyset. \quad (\text{A16})$$

Using the Euclidean norm, the minimum distance between the plane and the point ω is

$$\Delta_{m,n}(\omega) = \min_{\alpha \in \mathcal{R}_{m,n}} \|\alpha - \omega\|_2 = \frac{|m \cdot \omega - n|}{\|m\|_2}. \quad (\text{A17})$$

Thus, ω is (m, n) resonant to precision δ , whenever $\Delta_{m,n}(\omega) < \delta$, and we call the value

$$M(\omega, \delta) = \min \{ \|m\|_1 : \Delta_{m,n}(\omega) < \delta, m \in \mathbb{Z}^d \setminus \{0\}, n \in \mathbb{Z} \}, \quad (\text{A18})$$

the resonance order of ω .

As far as we know, there is no generalization of the $d = 1$ Farey tree result of Appendix A 2 to compute (A18) efficiently. (One could use the Kim–Ostlund tree to get resonance relations;⁵³ however, it is

not clear that this algorithm returns a minimal $\|m\|$.) Nevertheless, since there are finitely many $m \in \mathbb{Z}^d$ such that $\|m\|_1 \leq M$, a brute force computation is possible for modest values of M .¹⁰

To understand what resonance orders are “typical,” we computed the minimal resonance order (A18) for a set of equidistributed, random $\omega \in [0, 1]^2$ as a function of the precision δ .¹⁰ The resulting distribution of $\log(M)$ has a mean¹⁰

$$\langle \log_{10} M(\omega, \delta) \rangle = -0.334 \log_{10}(\delta) - 0.091. \quad (\text{A19})$$

Marklof^{48,49} has recently obtained theoretical results that are consistent with (A19). We find a standard deviation of

$$\sigma = 0.171.$$

As in the one-dimensional case, the standard deviation seems to be essentially independent of δ .

Since the cutoff (A7) gives rotation number calculations accurate to within 10^{-9} , we choose $\delta = 10^{-9}$. For this case, (A19) implies that $\langle \log_{10} M \rangle = 2.915$. We declare that a vector is nonresonant if

$$256 \leq M \leq 2673 \Rightarrow \text{“nonresonant,”} \quad (\text{A20})$$

corresponding to $2.407 < \log_{10}(M) < 3.427$, which is a range of approximately $\pm 3\sigma$ about the mean (A19). To test this criterion, we selected 10^4 randomly distributed values uniformly in $[0, 1]^2$ and found that 1.36% were incorrectly identified as resonant. Note that the distribution of log-orders for random vectors is not symmetric around the mean; in particular, $M < 256$ occurred 1.32% of the time and $M > 2673$ occurred 0.04% of the time.

We can further categorize the orbits that are determined to be resonant [those that fail criterion (A20)] by the rank of the resonance. Rank-two resonant orbits have frequencies on the intersection of a pair of different resonance lines, recall Fig. 4. That is, both of the components of the rotation vector are “rational.” These can be identified using the criterion

$$M \text{ fails (A20) and } \omega_1, \omega_2 \text{ fail (A15)} \Rightarrow \text{“periodic.”} \quad (\text{A21})$$

If a resonant orbit is not periodic, then it lies on a single resonance line and so has rank one. We will simply refer to such orbits as “resonant”; they typically are dense on topological circles. Thus, the criterion for a (rank-one) resonant orbit is

$$M \text{ fails (A20) but at least one of } \omega_1, \omega_2 \text{ satisfy (A15)} \Rightarrow \text{“resonant.”} \quad (\text{A22})$$

The criteria (A21) and (A22) are used to distinguish the orbit types for the 2D maps in Sec. IV.

TABLE II. The parameters ε and Ω for the orbits in Fig. 5, using the force (8) with amplitudes and phases for case (0) in Table III. The last two columns give the computed ω_T and dig_T using $T = 10^6$.

Label	ε	Ω	ω_T	dig_T
(a)	0.8	(0.2, 0.7)	(0.195 709 415 335 09, 0.704 569 417 667 74)	14.7505
(b)	0.8	(0.84, 0.835)	(0.839 470 290 894 69, 0.839 470 290 894 70)	15.2556
(c)	0.8	(0.5, 0.7)	(0.497 788 528 060 59, 0.703 300 860 156 10)	12.0529
(d)	1.5	(0.1, 0.8)	(0.074 250 240 472 12, 0.835 928 502 722 24)	14.3471
(e)	2.6	(0.7, 0.3)		4.0484
(f)	4.0	(0.24, 0.4)		2.5522

APPENDIX B: CRITICAL ε

In this appendix, we explain why $\varepsilon_{\text{crit}}$ (11) almost always exists for most choices of amplitudes a_i and phases ϕ_i . We first argue that typically there is some point (x_1, x_2) for which $\det(H) < 0$ for the matrix H in (10). First, if we choose $x_2 = -\phi_2$, then

$$\det(H(x_1, -\phi_2)) = a_1 a_4 \sin(2\pi(x_1 + \phi_1)) \sin(2\pi(\phi_4 - \phi_2)).$$

Therefore, if $a_1 a_4 \neq 0$ and $\phi_4 - \phi_2 \neq n\pi$ for some integer n , this determinant is nonzero and odd about $x_1 = -\phi_1$. Thus, $\det(H) < 0$ at some point. If $\phi_4 - \phi_2 = n\pi$, we can consider a similar argument upon choosing $x_1 = -\phi_3$ as long as $\phi_3 - \phi_1 \neq m\pi$ for some integer m . Equivalent arguments apply if $a_2 a_3 \neq 0$, as long as $\phi_4 - \phi_2 \neq n\pi$ or $\phi_3 - \phi_1 \neq m\pi$.

An exceptional case would be if both $\phi_4 - \phi_2 = n\pi$, $\phi_3 - \phi_1 = m\pi$. Now choose $x_1 = \frac{\pi}{2} - \phi_1$ and $x_2 = \frac{\pi}{2} - \phi_4$. Then

$$\begin{aligned} \det H &= a_1 a_4 \sin \frac{\pi}{2} \sin \frac{\pi}{2} \\ &\quad - a_2 a_3 \sin \left(\frac{\pi}{2} + \phi_3 - \phi_1 \right) \sin \left(\frac{\pi}{2} + \phi_2 - \phi_4 \right) \\ &= a_1 a_4 - a_2 a_3 \sin \left(\frac{\pi}{2} + n\pi \right) \sin \left(\frac{\pi}{2} - m\pi \right). \end{aligned} \quad (\text{B1})$$

Note that if m and n are both even or both odd (i.e., have the same parity), then at this point $H = a_1 a_4 - a_2 a_3$. Thus, as long as $a_1 a_4 - a_2 a_3 < 0$, $\det(H) < 0$ at this point. On the other hand, if $a_1 a_4 - a_2 a_3 > 0$, then use $x_2 = \frac{3\pi}{2} - \phi_2$, which flips the signs of both terms, again giving $\det(H) < 0$. If, however, m and n have the opposite parity, then at the point (B1) $\det(H) = a_1 a_4 + a_2 a_3$. If this is negative, we are done. Otherwise, use $x_2 = -\phi_2 + \frac{3\pi}{2}$, which flips the signs of both terms.

If none of the above cases hold, then $a_1 a_4 - a_2 a_3 = a_1 a_4 + a_2 a_3 = 0$, $\phi_4 - \phi_2 = n\pi$, $\phi_3 - \phi_1 = m\pi$, implying that $\det(H)$ is identically zero. But as long as the trace is nonzero, we can use a similar argument for the term that is linear in ε in (10) to show that $\varepsilon_{\text{crit}}$ exists.

Therefore, the only exception to the existence of $\varepsilon_{\text{crit}}$ is the case $a_1 = a_4 = 0$ and $a_2 a_3 = 0$, which gives trivial dynamics.

APPENDIX C: PARAMETERS FOR SEC. IV

This appendix gives the parameters for the computations in Sec. IV. The parameters ε and Ω for the images in Fig. 5 are shown in Table II. This also gives the computed ω_T for the regular orbits—cases (a)–(d), and the precision dig_T for each case. Table III

TABLE III. Amplitudes, phases, and $\varepsilon_{\text{crit}}$ for curves in Figs. 5–8 [case (0)] and in Fig. 9 [cases (0–7)].

Case	Param.	1	2	3	4	$\varepsilon_{\text{crit}}$
0	a_i	0.221 320 306 832 860	0.220 593 736 048 273	0.152 270 586 812 051	0.405 815 370 306 816	2.220 44
	ϕ_i	0.369 246 781 120 215	0.111 202 755 293 787	0.780 252 068 321 138	0.389 738 836 961 253	
1	a_i	0.406 588 842 221 655	0.062 715 680 327 705	0.179 066 359 898 821	0.351 629 117 551 819	2.2070
	ϕ_i	0.957 506 835 434 298	0.964 888 535 199 277	0.157 613 081 677 548	0.970 592 781 760 616	
2	a_i	0.211 681 398 612 178	0.317 651 811 580 494	0.375 591 536 887 180	0.095 075 252 920 149	2.4566
	ϕ_i	0.273 022 072 458 714	0.542 430 207 288 253	0.431 224 181 579 691	0.153 093 675 447 227	
3	a_i	0.012 536 281 513 538	0.465 737 538 631 897	0.503 609 970 119 032	0.018 116 209 735 533	2.0564
	ϕ_i	0.739 790 415 703 666	0.023 926 884 448 995	0.490 328 482 174 893	0.304 888 898 615 625	
4	a_i	0.760 566 444 256 527	0	0	0.239 433 555 743 473	1.3148
	ϕ_i	0.739 790 415 703 666	0.023 926 884 448 995	0.490 328 482 174 893	0.304 888 898 615 625	
5	a_i	0	0.760 566 444 256 527	0.239 433 555 743 473	0	2.3434
	ϕ_i	0.739 790 415 703 666	0.023 926 884 448 99	0.490 328 482 174 893	0.304 888 898 615 625	
6	a_i	0.007 280 035 519 179	0.942 703 650 246 408	0.039 647 117 954 398	0.010 369 196 280 015	5.2100
	ϕ_i	0.384 398 913 909 761	0.203 897 175 276 146	0.913 862 879 483 257	0.191 420 654 770 675	
7	a_i	0	0.352 156 017 226 267	0	0.647 843 982 773 733	1.5436
	ϕ_i	0.369 246 781 120 215	0.111 202 755 293 787	0.780 252 068 321 138	0.389 738 836 961 253	

gives amplitudes and phases for (8) used in Figs. 5–8 [case (0)] and in Fig. 9 (eight cases) along with the calculated values of $\varepsilon_{\text{crit}}$. For all of these parameter sets, $\|a\|_1 = 1$.

REFERENCES

- ¹V. Arnold, “Small denominators I: Mappings of the circumference onto itself,” *Izv. Akad. Nauk Ser. Mat.* **25**, 21–86 (1961).
- ²M. Jensen, P. Bak, and T. Bohr, “Transition to chaos by interaction of resonances in dissipative systems. I. Circle maps,” *Phys. Rev. A* **30**, 1960–1969 (1984).
- ³R. Ecke, J. Farmer, and D. Unger, “Scaling of the Arnold tongues,” *Nonlinearity* **2**, 175–196 (1989).
- ⁴C. Grebogi, E. Ott, and J. Yorke, “Are three-frequency quasiperiodic orbits to be expected in typical nonlinear dynamical systems?” *Phys. Rev. Lett.* **51**, 339 (1983).
- ⁵C. Grebogi, E. Ott, and J. Yorke, “Attractors on an N-torus: Quasiperiodicity versus chaos,” *Physica D* **15**, 354–373 (1985).
- ⁶S. Das, Y. Saiki, E. Sander, and J. Yorke, “Quasiperiodicity: Rotation numbers,” in *Foundations of Chaos Revisited: From Poincaré to Recent Advancement*, Understanding Complex Systems, edited by C. Skiadas (Springer, 2016), pp. 103–118.
- ⁷S. Das, Y. Saiki, E. Sander, and J. Yorke, “Quantitative quasiperiodicity,” *Nonlinearity* **30**, 4111 (2017).
- ⁸S. Das, Y. Saiki, E. Sander, and J. Yorke, “Solving the Babylonian problem of quasiperiodic rotation rates,” *Discrete Contin. Dyn. Syst.* **12**, 2279–2305 (2019).
- ⁹E. Sander and J. Meiss, “Birkhoff averages and rotational invariant circles for area-preserving maps,” *Physica D* **411**, 132569 (2020).
- ¹⁰J. Meiss and E. Sander, “Birkhoff averages and the breakdown of invariant tori in volume-preserving maps,” *Physica D* **428**, 133048 (2021).
- ¹¹J. Laskar, “Frequency analysis for multi-dimensional systems. Global dynamics and diffusion,” *Physica D* **67**, 257–281 (1993).
- ¹²S. Das and J. Yorke, “Super convergence of ergodic averages for quasiperiodic orbits,” *Nonlinearity* **31**, 491–501 (2018).
- ¹³T. Seara and J. Villanueva, “On the numerical computation of Diophantine rotation numbers of analytic circle maps,” *Physica D* **217**, 107–120 (2006).
- ¹⁴A. Luque and J. Villanueva, “Computation of derivatives of the rotation number for parametric families of circle diffeomorphisms,” *Physica D* **237**, 25992615 (2008).
- ¹⁵T. Seara and J. Villanueva, “Numerical computation of the asymptotic size of the rotation domain for the Arnold family,” *Physica D* **238**, 197–208 (2009).
- ¹⁶A. Luque and J. Villanueva, “Quasi-periodic frequency analysis using averaging-extrapolation methods,” *SIAM J. Dyn. Syst.* **13**, 1–46 (2014).
- ¹⁷J. Villanueva, “A new averaging-extrapolation method for quasi-periodic frequency refinement,” *Physica D* **438**, 133344 (2022).
- ¹⁸L. A. Rmaileh, “Characterizing islands in area-preserving maps,” Ph.D. thesis (Weizmann Institute of Science, Rehovot, Israel, 2015).
- ¹⁹R. MacKay, “Rotation interval from a time series,” *J. Phys. A* **20**, 587–592 (1987).
- ²⁰L. Alsedà and S. Borrós-Culler, “An algorithm to compute rotation intervals of circle maps,” *Commun. Nonlinear Sci. Numer. Simul.* **102**, 105915 (2021).
- ²¹K. Polotzek, K. Padberg-Gehle, and T. Jäger, “Set-oriented numerical computation of rotation sets,” *J. Comput. Dyn.* **4**, 119–141 (2017).
- ²²J. Sanchez, M. Net, and C. Simó, “Computation of invariant tori by Newton-Krylov methods in large-scale dissipative systems,” *Physica D* **239**, 123–133 (2010).
- ²³A. Haro, M. Canadell, J.-L. Figueras, A.-L. Josep, and M. Mondelo, *The Parameterization Method for Invariant Manifolds from Rigorous Results to Effective Computations* (Springer International, 2016).
- ²⁴D. Blessing and J. D. M. James, “Weighted Birkhoff averages and the parameterization method,” *SIAM J. Dyn. Syst.* **23**(3), 1766–1804 (2024).
- ²⁵M. Misiurewicz and K. Zieman, “Rotation sets for maps of tori,” *J. London Math. Soc.* **s2-40**, 490–506 (1989).
- ²⁶R. MacKay, “Mode-locking and rotational chaos in networks of oscillators: A mathematical framework,” *J. Nonlinear Sci.* **4**, 301–314 (1994).

- ²⁷A. Katok and B. Hasselblatt, *Introduction to the Modern Theory of Dynamical Systems*, Encyclopedia of Mathematics and Its Applications Vol. 54 (Cambridge University Press, Cambridge, 1999).
- ²⁸J. Guckenheimer and P. Holmes, *Nonlinear Oscillations, Dynamical Systems, and Bifurcations of Vector Fields*, Appl. Math. Sci. Vol. 42 (Springer-Verlag, New York, 2002).
- ²⁹S. Kim, J. Guckenheimer, and R. MacKay, “Resonance regions for families of torus maps,” *Nonlinearity* **2**, 391–404 (1989).
- ³⁰H. Bass, E. Connell, and D. Wright, “The Jacobian conjecture: Reduction of degree and formal expansion of inverse,” *Bull. Am. Math. Soc.* **7**, 287–330 (1982).
- ³¹R. S. MacKay and C. Tresser, “Transition to topological chaos for circle maps,” *Physica D* **19**, 206–237 (1986).
- ³²R. S. MacKay and C. Tresser, “Erratum transition to topological chaos for circle maps,” *Physica D* **29**, 427 (1988).
- ³³H. E. Nusse, J. A. Yorke, and E. J. Kostelich, *Dynamics: Numerical Explorations*, edited by F. John, J. E. Marsden, and L. Sirovich, Applied Mathematical Sciences Vol. 101 (Springer US, New York, 1994).
- ³⁴J. L. Figueras, A. Haro, and A. Luque, “Effective bounds for the measure of rotations,” *Nonlinearity* **33**, 700–741 (2020).
- ³⁵G. Swiateck, “Rational rotation numbers for maps of the circle,” *Commun. Math. Phys.* **119**, 109–128 (1988).
- ³⁶K. Khanin, “Universal estimates for critical circle mappings,” *Chaos* **1**, 181186 (1991).
- ³⁷M. Ding, C. Grebogi, and E. Ott, “Evolution of attractors in quasiperiodically forced systems: From quasiperiodic to strange nonchaotic to chaotic,” *Phys. Rev. A* **39**, 2593–2598 (1989).
- ³⁸J. Llibre and R. MacKay, “Rotation vectors and entropy for homeomorphisms of the torus isotopic to the identity,” *Ergod. Theory Dyn. Syst.* **11**, 115–128 (1991).
- ³⁹C. Baesens, J. Guckenheimer, S. Kim, and R. MacKay, “Three coupled oscillators: Mode-locking, global bifurcations and toroidal chaos,” *Physica D* **49**, 387–475 (1991).
- ⁴⁰H. Osinga, J. Wiersig, P. Glendinning, and U. Feudel, “Multistability in the quasiperiodically forced circle map,” *Int. J. Bifurcation Chaos* **11**, 3085–3105 (2001).
- ⁴¹J. Stark, U. Feudel, P. Glendinning, and A. Pikovsky, “Rotation numbers for quasiperiodically forced monotone circle maps,” *Dyn. Syst.* **17**, 1–28 (2002).
- ⁴²T. Jäger and J. Stark, “Towards a classification for quasiperiodically forced circle homeomorphisms,” *J. London Math. Soc.* **73**, 727–744 (2006).
- ⁴³P. Glendinning, T. Jäger, and J. Stark, “Strangely dispersed minimal sets in the quasiperiodically forced Arnold circle map,” *Nonlinearity* **22**, 835–854 (2009).
- ⁴⁴J. D. Meiss and E. Sander, “Resonance and weak chaos in quasiperiodically-forced circle maps,” *Comm. Nonlinear Sci. Numer. Simulat.* **142**, 108562 (2025).
- ⁴⁵J. Yamagishi and K. Kaneko, “Chaos with a high-dimensional torus,” *Phys. Rev. Res.* **2**, 023044 (2020).
- ⁴⁶S. Kim and S. Ostlund, “Renormalization of mappings of the two-torus,” *Phys. Rev. Lett.* **55**, 1165–1168 (1985).
- ⁴⁷H. Chen and A. Haynes, “Expected value of the smallest denominator in a random interval of fixed radius,” *Int. J. Number Theory* **19**, 1405–1413 (2023).
- ⁴⁸J. Marklof, “The log moments of smallest denominators,” *Zenodo* **24**, 1–13 (2024).
- ⁴⁹J. Marklof, “Smallest denominators,” *Bull. London Math. Soc.* **56**, 1920–1938 (2024).
- ⁵⁰A. Kachurovskii, “The rate of convergence in ergodic theorems,” *Russ. Math. Surv.* **51**, 653 (1996).
- ⁵¹U. Krengel, “On the speed of convergence in the ergodic theorem,” *Monatsh. Math.* **86**, 3–6 (1978).
- ⁵²M. Ruth and D. Bindel, “Finding Birkhoff averages via adaptive filtering,” *Chaos* **34**, 123109 (2024).
- ⁵³P. Ashwin, J. Guaschi, and J. Phelps, “Rotation sets and phase-locking in an electronic three oscillator system,” *Physica D* **66**, 392–411 (1993).